



HAL
open science

**AlN as an actuation material for MEMS applications.
The case of AlN driven multilayered cantilevers**

Alexandru Andrei, Katarzyna Krupa, Michal Jozwik, Patrick Delobelle,
Laurent Hirsinger, Christophe Gorecki, Lukasz Nieradko, Cathy Meunier

► **To cite this version:**

Alexandru Andrei, Katarzyna Krupa, Michal Jozwik, Patrick Delobelle, Laurent Hirsinger, et al.. AlN as an actuation material for MEMS applications. The case of AlN driven multilayered cantilevers. Sensors and Actuators A: Physical , 2008, 141 (2), pp.565-576. 10.1016/j.sna.2007.10.041 . hal-00350132

HAL Id: hal-00350132

<https://hal.science/hal-00350132>

Submitted on 16 Jul 2024

HAL is a multi-disciplinary open access archive for the deposit and dissemination of scientific research documents, whether they are published or not. The documents may come from teaching and research institutions in France or abroad, or from public or private research centers.

L'archive ouverte pluridisciplinaire **HAL**, est destinée au dépôt et à la diffusion de documents scientifiques de niveau recherche, publiés ou non, émanant des établissements d'enseignement et de recherche français ou étrangers, des laboratoires publics ou privés.

AlN as an actuation material for MEMS applications

The case of AlN driven multilayered cantilevers

Alexandru Andrei^a, Katarzyna Krupa^a, Michal Jozwik^a, Patrick Delobelle^{b,*},
Laurent Hirsinger^b, Christophe Gorecki^a, Lukasz Nieradko^a, Cathy Meunier^c

^a LOPMD, FEMTO-ST, UMR CNRS 6174, University of Franche Comté, 16 route de Gray, 25000 Besançon, France

^b LMARC, FEMTO-ST, UMR CNRS 6174, University of Franche Comté, 24 chemin de l'Épitaphe, 25000 Besançon, France

^c CREST, FEMTO-ST, UMR CNRS 6174, University of Franche Comté, 4 place Tharradin, 25200 Montbéliard Cedex, France

This paper treats a wide range of subjects related to the use of AlN as actuation layer in MEMS, from its deposition conditions to accurate interferometric device characterization and physical parameters extraction. The case of AlN driven multilayered cantilevers has been considered. Parameters such as Young's modulus associated to the (0 0 2) orientation of the crystallites, residual thin film stresses, thermal expansion coefficient α and piezoelectric coefficient d_{31} have been calculated using non approximated equations able to take into account multiple film stacking. The well oriented thin films exhibit approximately the same properties as the bulk material.

Keywords: AlN; Piezoelectric; Beams; MEMS

1. Introduction

Aluminium nitride (AlN) is a III–V large direct band gap semiconductor material with appealing properties in a wide range of fields. Its piezoelectric properties associated with high ultrasonic velocity, good thermal stability and low temperature deposition (below 400 °C) compatible with the integrated circuits post-processing made it a promising candidate for GHz-band surface acoustic wave (SAW) [1,2] and bulk acoustic wave filters (BAW) [3,4]. Besides the ever-growing wireless communication market, AlN has also been used for sensing purposes in pressure, gravimetric and even chemical sensors based on lamb-wave propagation over AlN/silicon membranes [5,6]. For actuation purposes, PZT sol–gel films have been preferably used because of their high piezoelectric coefficients (around nine times greater than those of AlN) and the possibility to be deposited with great thicknesses. However, AlN still represents a good alternative for MEMS actuation [7], offering a great number of advantages [8]. Besides its inte-

grated circuits post-processing compatibility, due to the low deposition temperatures, AlN has an excellent chemical stability, a dielectric constant 100 times smaller than PZT ones, a high breakdown field (>800 kV/cm) and is a non ferroelectric material that does not require poling. Therefore, AlN films are competitive in actuation applications where low dielectric loss, low thermal drift and high signal-to-noise ratios are required. The aim of the present work is the development of high quality AlN driven cantilevers that will be used in more complex MEMS, such as the on-chip near-field optical microscope proposed by Bargiel et al. [9]. Besides the actual device processing, the study focused on the stress and crystallographic orientation control of the AlN film. In general, (002) oriented AlN films are easily obtained by physical vapour deposition (PVD) methods such as sputtering. However, the (002) oriented AlN films have poor electromechanical properties which can be substantially improved if an (100) orientation is achieved [10]. There are many parameters influencing the AlN film growth [10–16], such as the distance between the Al target and the substrate, the gas pressure, the sputtering power and moreover. In this paper we study the influence of the bottom metal electrode on the internal stress, the crystallographic and the piezoelectric properties of the AlN film deposited on it. The relationship

* Corresponding author. Tel.: +33 3 81 66 60 13; fax: +33 3 81 66 67 00.

E-mail address: patrick.delobelle@univ-fcomte.fr (P. Delobelle).

between the residual stress and the sputtering time has also been reported.

2. Experimental procedure

2.1. Sample fabrication

The AlN driven micro-beams were fabricated on 380- μm thick, 3 in. (1 0 0) oriented Si wafers. The process flow is shown in Fig. 1(a). After realizing a 15 μm thick Si membrane by KOH etch on the bottom side of the wafer (step 1), three thin layers have been successively deposited on the top side: two CrNi PVD metal layers (0.15 μm at step 2 and 0.35 μm at step 4) separated by the AlN film. The Cr_{50%}Ni_{50%} alloy has been sputtered on a substrate, heated (200 °C) at 230 W (0.5 A) using a 0.93 Pa Ar gas pressure. The AlN has been deposited (step 3) in a pulsed reactive dc sputtering machine on a non heated substrate placed at 70 mm from the Al target, with an input power of 650 W, a Ar/N₂ gas ratio of 0.65 sccm/6 sccm and a pressure of 0.65 Pa.

These conditions led to a deposition rate around 17 nm/min, which is in agreement with the results of Kusaka et al. [13]. Two different wafers have been processed, with final AlN film thicknesses of 1 μm (wafer 1) and 1.4 μm (wafer 2). The substrate temperature being only dependent on the self-heating plasma, its value never reached 130 °C at the end of the AlN film depo-

sition. The top CrNi electrode patterned at step 4, has been used as a hard mask during the AlN and silicon etching (steps 5 and 7). An intermediary process step allowed the deposition and patterning of 0.5 μm thick aluminium pads that have been used for wire bonding.

The AlN has been etched using a humid base solution. The silicon, which was not protected by the CrNi hard mask, was etched by reactive ion etching transforming the initial Si membranes into an array of free standing cantilevers. They had a constant width of 50 μm and variable lengths from 200 μm up to 900 μm . Note that the precise thickness of the beams (\cong 15 μm) has been determined by SEM. The layout of the 200 μm long cantilever array is shown in Fig. 1(b). The actuation of the cantilevers is done by applying a voltage between the upper and the bottom metal electrodes. Fig. 2 presents a SEM picture of the final device, diced and connected to the package.

Before the fabrication of the devices, a series of test structures has been realized in order to measure the stress in the films and the influence of the bottom electrode nature on the stress in the AlN film. These test structures were arrays of 13 μm thick silicon cantilevers, 0.5 mm wide, with lengths varying from 0.5 mm up to 3.5 mm. Two bottom electrodes have been tested: 0.16 μm thick CrNi and 0.24 μm thick Pt films. The CrNi has been deposited using the same conditions than for the devices, while the Pt has been sputtered on a non biased, non heated substrate at 120 W (0.22 A) using a 1.1 Pa Ar gas. After

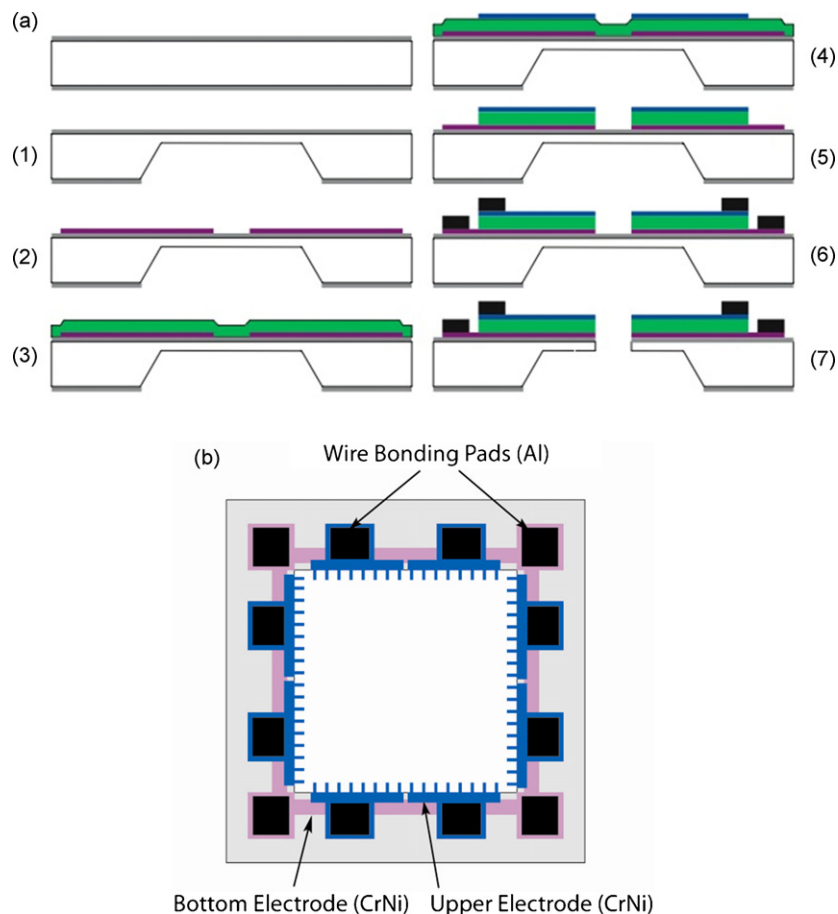


Fig. 1. Cantilever process flow chart (a) and specific layout (b).

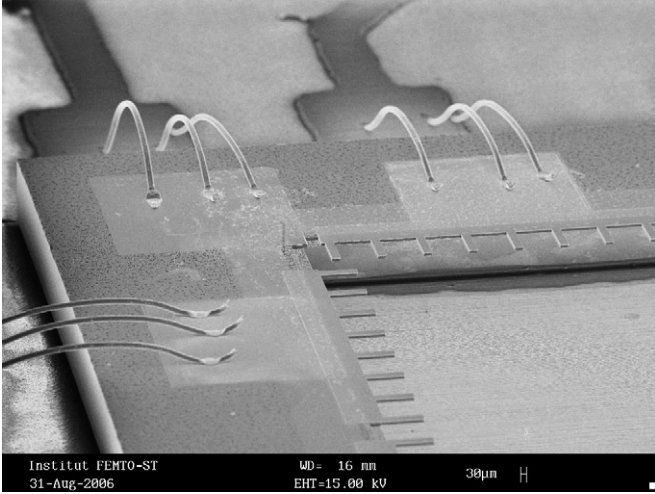


Fig. 2. SEM picture of a packaged chip.

measuring the cantilever bending, a $0.8 \mu\text{m}$ thick AlN layer has been deposited using the same conditions than for the devices.

2.2. Interferometric measurements

Both test structures and AlN driven cantilevers have been characterized using a previously validated measurement set-up based on a Twyman-Green interferometer [16,17]. This experimental set-up allowed both static and dynamic measurements of the samples. The use of a thermo-electrical module allowed us to fix the sample temperature anyway between 15°C and 60°C with an 0.01°C accuracy. The static measurements consisted in cantilever deflection measurements when no voltage or a certain dc voltage (between -15 and $+15$ V) was applied between the top and bottom metal electrodes. Five frames of interferometric intensity data taken at 90° relative phase shifts were used with a phase shifting algorithm in order to obtain a highly accurate measurement of the cantilever profile (20 nm accuracy on vertical displacement) [16,17].

Fig. 3 shows such a measured profile of three $800 \mu\text{m}$ long adjacent cantilevers with no applied voltage ($1.4 \mu\text{m}$ AlN film thickness wafer). For the dynamic measurements, an 8 PP sinusoidal signal was applied to the cantilevers, their first resonance frequency being determined by a time average technique [16]. As these measurements have been used for physical parameter calculation, such as internal stress or piezoelectric coefficient values, the precise knowledge of the thin film and silicon thicknesses was essential. Therefore, for each of the devices present over the wafer, the metal electrodes and AlN thicknesses have been measured by mechanical profilometry (few nm accuracy). Each cantilever silicon thickness has been measured by SEM with a $0.2 \mu\text{m}$ accuracy.

2.3. Nanoindentation measurements

Nanoindentation tests were performed on the AlN films of the test structures using a nanoindenter II^S (Nano-Instruments) with a Berkovich tip. The study was conducted following the

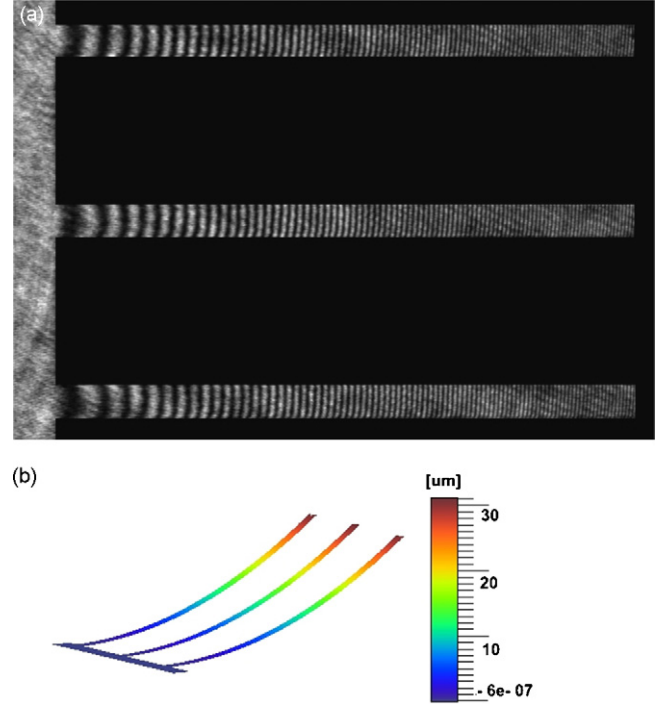


Fig. 3. An example of the five phase shifted interferograms used for the cantilever profile measurement (a) and the corresponding final 3D profile (b).

continuous contact stiffness measurement procedure [18] with a frequency of 45 Hz and an indenter vibration amplitude of 1 nm during the penetration of the tip into the sample. It allowed the determination of the indentation modulus $M_{(hkl)}$ and the hardness $H_{b(hkl)}$ for AlN deposited on Pt and CrNi electrodes.

For each tested sample, the measurement sequence consists on 15 indents with a $50 \mu\text{m}$ space between them, on three or four different zones of the film ($15 \times 3/4$ indents), with a maximum penetration depth of $h_{\text{max}} = 200$ nm and covering an area of $200 \mu\text{m} \times 200 \mu\text{m}$ for each zone. For $h_{\text{max}} = 200$ nm the maximum load range value is about 15–18 mN. The penetration speed was not constant but increased with depth from $1-8 \text{ nm s}^{-1}$. The thickness of the tested films is about $0.8 \mu\text{m}$.

2.4. AFM measurements

The standard deviation of nanoindentation measurements is strongly related to surface roughness [19,20], then the film's roughness was evaluated with an atomic force microscope (PSIA, XE 150) in non contact mode. An area of $7 \mu\text{m} \times 7 \mu\text{m}$ was scanned at three different positions in the surface in order to make sure that the images taken in AFM are representative of the film surface. We found an average roughness R_{ms} of 2.4 ± 0.4 nm for the AlN deposited on the CrNi electrode and $R_{\text{ms}} = 2.0 \pm 0.3$ nm for the AlN deposited on the Pt electrode.

2.5. X-ray diffraction measurements

We use Cu $K\alpha$ radiations on X'Pert MPD PANalytical system, to obtain $\theta-2\theta$ data in a Bragg Brentano geometry with a

step size of 0.02° (2θ) and a step time of 5 s. Highly textured AlN films are observed and Ω scans are taken on the (002) AlN diffraction line at $\theta = 18^\circ$ with a step size of 0.04° (2θ), a step time of 2 s and $\Delta\Omega = 20^\circ$. For the size calculation, sample function is extracted from raw data by de-convolution with a $\delta\theta = 0.01^\circ$ resolution. Scherrer relation is used with a silicon standard.

3. Equations for multilayered cantilevers

Several theoretical models regarding stress analysis of single layer of thin film deposited on an elastically isotropic substrate have been developed since the first works of Stoney in 1909 [21–24]. Stress models for multiple elastic layers of thin films or multilayered structure were introduced in the 1980s. Moreover, the mechanics of a heterogeneous piezoelectric bimorph under the influence of an external applied electric field has been analysed by Smits and Choi [25] and the extension of these results to different configurations of multilayer piezoelectric actuator with bending deformation has been considered by different authors [26–28].

In previous works [29,30], the composite laminate theory (CLT) applied to a three layers cantilever with one piezoelectric material considering the linear constitutive equations for the piezoelectric material allowed to establish the relations giving the deflection of the structure as a function of the applied or residual stress, the applied voltage and the temperature. These relations are used in the present paper (Eqs. (1)–(8)).

3.1. Internal stress related cantilever deflection

The use of the same metal (CrNi) for the top and bottom electrodes, allowed us to consider, for simplification reasons, that the silicon cantilever has only two films on its surface: the AlN film and a metal electrode film with a thickness equal to the sum of the top and bottom electrodes thicknesses. The stress in the AlN and metal films are resulting in a mechanical deflection δ_m of the cantilever that can be written as:

$$\delta_m = \frac{3(1-\nu) E_s h_s^2 - (E_f h_f + E_e h_e)(h_e + h_f)}{E_{eq} h_{eq}^2} \frac{E_s h_s + E_f h_f + E_e h_e}{E_s h_s + E_f h_f + E_e h_e} L^2 \sigma_0 \quad (1)$$

with the global stress σ_0 :

$$\sigma_0 = \frac{\sigma_f h_f + \sigma_e h_e + \sigma_s h_s}{h_{eq}} \quad (2)$$

and where E_i , h_i and σ_i with $i = s, f, e$ are the Young modulus, the thickness and the stress of the silicon substrate (s), the AlN film (f) and the metal electrodes (e). L represents the cantilever's length and ν the Poisson coefficient taken equal for all the materials. The equivalent thickness h_{eq} is equal to the sum of h_s , h_f and h_e while E_{eq} represents the equivalent modulus that can be written as:

$$E_{eq} = \frac{K_1 + K_2 + K_3 + K_4 + K_5}{(E_f h_f + E_s h_s + E_e h_e) h_{eq}^3} \quad (3a)$$

with

$$K_1 = E_f^2 h_f^4 + E_s^2 h_s^4 + E_e^2 h_e^4 \quad (3b)$$

$$K_2 = 2E_s E_e h_s h_e (2h_s^2 + 2h_e^2 + 3h_s h_e) \quad (3c)$$

$$K_3 = 2E_f E_e h_f h_e (2h_f^2 + 2h_e^2 + 3h_f h_e) \quad (3d)$$

$$K_4 = 2E_f E_s h_f h_s (2h_s^2 + 2h_f^2 + 3h_s h_f) \quad (3e)$$

$$K_5 = 12E_s E_f h_s h_f h_e h_{eq} \quad (3f)$$

It is interesting to notice that a first order development of the Eq. (3), considering $h_e = 0$ in the Eqs. (1), (2) and (3), gives a generalized writing of the Stoney equation:

$$\sigma_f = \frac{E_s h_s^2 \delta_m}{3(1-\nu) h_f L^2} \left[1 + 4 \underbrace{\frac{E_f h_f}{E_s h_s}}_A \left(1 + \underbrace{\frac{3h_f}{2h_s}}_B \right) \right] \quad (4)$$

Eq. (4) is in good agreement with the relation established by Röll [20], only the B term differs.

In this study, using the Stoney equation (first term in Eq. (4)) would have introduced a significant under-estimation of the stress in the film, since the values of the terms A and B are 0.78 and 0.11, respectively. In these case, $E_f/E_s \cong 2.6$ and $h_f/h_s \cong 7.5 \times 10^{-2}$.

3.2. Piezoelectric induced deflection and first resonance frequency

Under an applied voltage U , the linear piezoelectric properties of the AlN film will result in an additional deflection δ_p that can be related to the AlN piezoelectric coefficient d_{31} by:

$$\delta_p = -\frac{3}{E_{eq} h_{eq}^2} \frac{E_f (E_s h_s + E_e h_e)}{E_s h_s + E_f h_f + E_e h_e} d_{31} L^2 U \quad (5)$$

This expression agrees with those developed by Wang et al. [26] for a symmetric triple layer bender. Putting in the above equations $h_e = 0$ leads to the classic equations for a piezoelectric film deposited on a thick cantilever [25,29,30].

The first resonance frequency value of a three-layer bender can be written as:

$$f_1 = \frac{p_1^2}{4\pi\sqrt{3}} \frac{h_{eq}}{L^2} \sqrt{\frac{E_{eq}}{\rho_{eq}}} \quad (6)$$

where h_{eq} is the equivalent thickness, E_{eq} is the equivalent Young modulus above defined (Eq. (3)). The p_1 term value is 1.875 and the equivalent density term ρ_{eq} is equal to:

$$\rho_{eq} = \frac{\rho_s h_s + \rho_f h_f + \rho_e h_e}{h_{eq}} \quad (7)$$

3.3. The influence of the temperature

Under a thermal loading ΔT , the corresponding deflection δ_{Th} of the bender is related to the thermal expansion coefficients

of the different layers α_s , α_f and α_e , by the following equation:

$$\delta_{Th} = 3 \frac{[E_s h_s^2 - (E_f h_f + E_e h_e)(h_e + h_f)] [\alpha_s (E_f h_f + E_e h_e) - (E_f \alpha_f h_f + E_e \alpha_e h_e)]}{E_{eq} h_{eq}^3 (E_f h_f + E_s h_s + E_e h_e)} L^2 \Delta T \quad (8)$$

4. Results and interpretations

4.1. XRD results

Fig. 4a shows the typical X-rays diffraction spectrum of AlN films deposited on CrNi and Pt electrodes. The crystallites of the AlN film are perfectly (002) oriented for the CrNi electrode; the c axis of the hexagonal structure is perpendicular to the substrate surface. The different peaks of the CrNi have been identified. However, the presence of additional peaks (noted with star in Fig. 4a) corresponds to additional compounds in relation with the employed target (may be oxy-nitride of CrNi). For Pt electrode, oriented (111), the direction (002) of the crystallites is always the more pronounced but the flat hill at about 45° indicates the presence of an amorphous part. In this case, the morphology of the films is more complex; well (002) oriented crystallites embedded in amorphous phase.

The FWHM of the Ω scan of the (002) plane, Fig. 4b, is smaller for Pt electrode (1.37°) than for CrNi (2.68°) which indi-

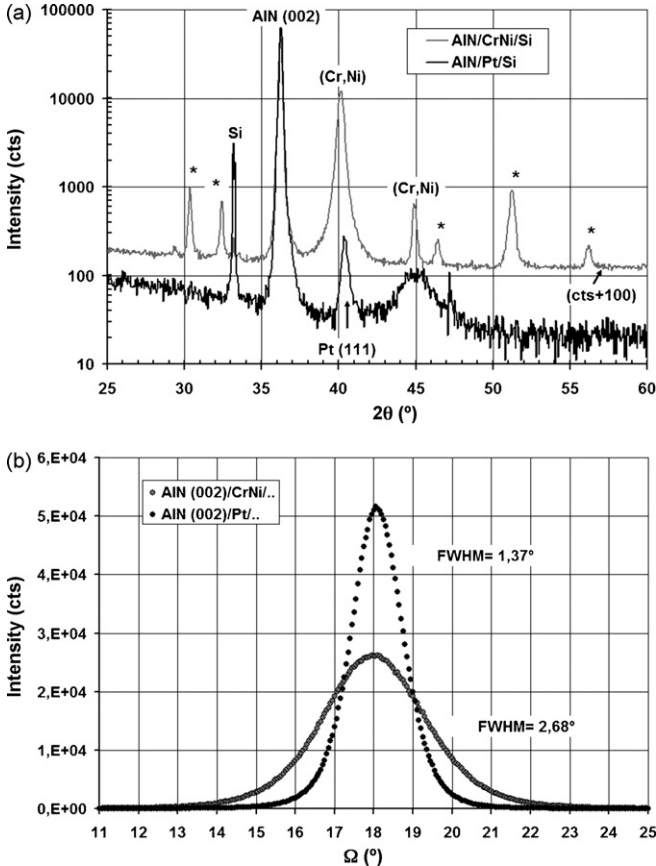


Fig. 4. Typical X-ray diagrams for AlN on CrNi and Pt (a) FWHM of the Ω scan of the (002) plane (b).

cates a better (002) orientation for the Pt electrode. These different observations, in relation with the deposition conditions previously mentioned are consistent with those of Ishihara et al. [10].

It can be concluded that the CrNi electrode is more convenient for MEMS applications, since the AlN deposited on it had only one better (002) orientation.

4.2. Indentation modulus values

In nano-indentation, the $M_{(hkl)}$ modulus, measured on a single crystal, whose normal to the surface has director cosine α_i is given by [31,32]

$$M_{(hkl)} = 16\pi^2 \left[\int_0^{2\pi} \alpha_m \beta_{km}^{-1} (C_{ij} \gamma) \alpha_k d\gamma \right]^{-1}$$

with $M_{(hkl)} = \left[\frac{1}{M_r} - \left(\frac{1 - \nu^2}{E} \right)_{ind} \right]^{-1}$

and $M_r = \frac{\sqrt{\pi}}{2\beta\sqrt{A}} \frac{dP}{dh}$, $A(h_c) = 24.5h_c^2 + \sum_{n=1}^4 (a_n h_c^{1/n})$,

and $h_c = h - \varepsilon \left(\frac{P}{S} \right)$ (9)

A is the projected contact area, P the applied load, $S = (dP/dh)$ the unloading stiffness measured at the depth of penetration h , $\beta = 1.034$ and $\varepsilon = 0.72$ for the Berkovich's tip. $(E/(1 - \nu^2))_{ind}$ is the reduced modulus of the diamond indenter, γ is the angle in surface plane and $\beta_{km}(C_{ij}, \gamma)$ a very complicated matrix function of the elastic stiffness C_{ij} and γ [31,32].

In our case, depending on the crystallite orientation occurring in the deposition process as mentioned before, the $M_{(hkl)}$ modulus determined by nano-indentation should not be constant. The measured hardness is given by:

$$H_{b(hkl)} = \frac{P}{A} \quad (10)$$

No general analytic solution of Eq. (9) exists. However, for some configurations, *approximated* solutions are available and give very close results to numerical solutions resulting from Eq. (9). For an hexagonal symmetry (isotropic transverse ($C_{66} \cong C_{11} - C_{12}/2$)) it is shown [33] that:

$$M_{\langle 001 \rangle} = \frac{2}{\sqrt{(C_{11}/C_{11} C_{33} - C_{13}^2)(1/C_{44} + 2/\sqrt{C_{11} C_{33} + C_{13}})}} \quad (11)$$

$$M_{\langle 100 \rangle} = M_{\langle 110 \rangle} = \sqrt{(C_{11}^2 - C_{12}^2/C_{11})\sqrt{C_{11}/C_{33}} M_{\langle 001 \rangle}} \quad (12)$$

Between these two values, there is no analytical solution, only approximated numerical solutions [34].

Different values of the C_{ij} elastic constants of sputtered AlN thin films [35] and epitaxial AlN films grown at high temperature [36,37] are reported in the literature.

Table 1
Values of the C_{ij} elastic constants ($C_{12} = C_{11} - 2C_{66}$) and the $M_{(hkl)}$ indentation modulus of AlN material

| | C_{11} | C_{13} | C_{33} | C_{44} | C_{66} | $M_{(001)}$ | $M_{(100)}$ | Ref. |
|------------------------|----------|----------|----------|----------|----------|-------------|-------------|------|
| Sputtered high quality | 360 | 123 | 410 | 116 | 119 | 342 | 319 | [35] |
| Low quality | 326 | 122 | 401 | 99 | 108 | 316 | 286 | [35] |
| Epitaxial | 345 | 120 | 395 | 118 | 110 | 335 | 306 | [36] |
| Bulk | 396 | 108 | 373 | 116 | 129.5 | 329 | 344 | [37] |

It has been reported that the values of the elastic constants of the sputtered AlN films exhibit an appreciable dependence on the micro-structural properties of the films, which are strongly affected by the deposition conditions. Table 1 gives the C_{ij} values and the corresponding values of $M_{(001)}$ and $M_{(100)}$ calculated with Eqs. (11) and (12).

Fig. 5a and b represent the evolution of mean values of the $M_{(hkl)}$ modulus and hardness $H_b(hkl)$ versus the reduced indentation depth h/h_f for the two kinds of electrode (CrNi/Si and Pt/Si) and for AlN on glass [38]. In order to study the evolution of these parameters with the micro-structural morphology of the studied films, taking account the presence of the substrate, the analysis of measurements at low indentation depths, typically for $h/h_f \leq 10\%$ [39,40] is required. These results are analysed for $h = 25, 50$ and 75 nm ($3.1 \leq h/h_f \leq 9.4\%$). The indentation modulus $M_{(hkl)}$ is a decreasing function of h/h_f (Fig. 5a) since $M_{(hkl)}(\text{AlN}) > M_{(100)}(\text{Si}) = 189$ GPa and $M_{(hkl)}(\text{AlN}) > M(\text{SiO}_2) = 80$ GPa.

For $h/h_f \approx 0$, the calculated mean values are $M_{(hkl)} = 340 \pm 10$ GPa for AlN/CrNi/Si, $M_{(hkl)} = 305 \pm 10$ GPa for AlN/Pt/Si and $M_{(hkl)} = 270 \pm 10$ GPa for AlN on glass. As for the hardness, $H_b(hkl)$ is an increasing function of the reduced indentation depth for $h/h_f \leq 10\%$ and then a slightly decreasing function of h/h_f since the hardness of the silicon is lower than those of the films $H_b(\text{AlN}) > H_b(\text{Si}) = 13.5$ GPa.

However, as shown by Xue et al. [41], for the small indentation depths, the increase of the measured hardness is due to the spherical shape of the indenter tip whose radius is in the order of 400 nm in the present study. Thus, only the values for $h/h_f \geq 10\%$ have to be considered as the Berkovich hardness of the films. For the three different substrates, the mean value of the AlN film hardness is around $H_b(hkl) \approx 26.0 \pm 1.5$ GPa. However, the relative standard deviation σ_E/E_{mean} (or σ_H/H_{mean}), where E_{mean} is the mean value of the Young's modulus of an isotropic material and σ_E the standard deviation determined over more than 25 indents [19], is related to the dimensionless parameter R_{ms}/h by the following equation [19,20]:

$$\frac{\sigma_E}{E_{\text{mean}}} = \alpha \left(\frac{R_{\text{ms}}}{h} \right)^m \quad (13)$$

For many metallic films deposited by sputtering technique, α and m have already been identified, $\alpha = 0.346$ and $m = 0.64$ [20]. Taking into account the measured values of R_{ms} ($2 < R_{\text{ms}} < 2.4$ nm), $\sigma_E/E_{\text{mean}} = \sigma_E/(1 - \nu^2)M_{(hkl)}$ (with $\nu = 0.25$) should approximately be equal to 7% and 5% for $h = 25$ and 50 nm, respectively. The experimental values are 11 and 7% for AlN/CrNi, 18 and 12% for AlN/glass and 35 and 24% for AlN/Pt. They are greater than those estimated with Eq. (13),

the multiplicative factor is about 1.4, 2.4 and 5.2, respectively. As shown on different PZT thin films [42,43] this factor can be considered as an indicator of the degree of the crystallite disorientation. This is in accordance with the XRD spectrums shown in Fig. 4: for well oriented crystallites, AlN/CrNi with (002) orientation, there is a fairly good agreement between the

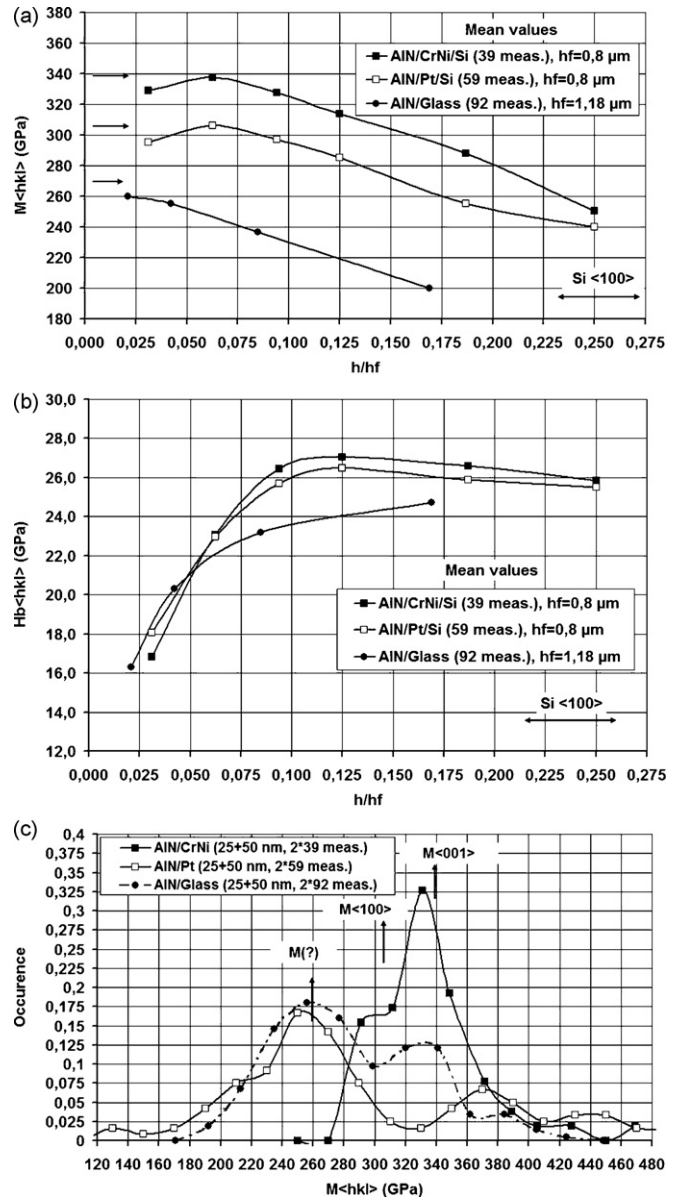


Fig. 5. Evolution of the indentation modulus $M_{(hkl)}$ (a) and the hardness $H_b(hkl)$ (b) as a function of the reduced depth for AlN deposited on Pt, CrNi and glass substrates. Histograms of the $M_{(hkl)}$ values (c).

calculation and the experimental values, factor 1.4. However, for more polycrystalline films, AlN/glass with (002) orientation [38] and AlN/Pt with simultaneous (002) orientation and amorphous phase the factor is equal to 2.4 and 5.2, respectively. To analyse the signification of the values of this factor, the histograms of the measured values of $M_{(hkl)}$, for $h = 25$ and 50 nm, and for each tested film are reported in Fig. 5c. For well oriented crystallites, (002) for AlN/CrNi (factor 1.4), there is only one peak centred at $M_{(hkl)} = 332$ GPa, close to the mean value and corresponding to $M_{(001)}$ calculated from the C_{ij} values of high quality sputtered films ($M_{(001)} = 342$ GPa) and epitaxial films ($M_{(001)} > 335$ GPa), Table 1.

However, for AlN on glass (factor 2.4 and a mean value equal to 270 GPa), there is two well defined peaks, the first one centred at $M_{(hkl)} = 335$ GPa and corresponding to the (002) orientation, as for AlN/CrNi film, and a second one at $M_{(hkl)} = 260$ GPa. For AlN/Pt, (factor 5.2 and a mean value equal to 305 GPa), there is also two well defined peaks at 370 and 260 GPa. The first one is certainly due to the very well (002) oriented crystallites (Fig. 4b). Concerning the peak at 260 GPa ($E = 244$ GPa for $\nu = 0.25$) and the corresponding value of the hardness $H_{b(hkl)} = 17$ GPa, these values seem too high to be attributed to the amorphous phase ($E \cong 140$ GPa, $H_b = 9.2$ GPa [44] and $80 < E < 220$ GPa, $3.5 < H_b < 20$ GPa [45]). However, these values are more consistent with those of the crystalline AlON phase obtained on Si and glass heat substrates, $E = 261$ GPa, $H_b = 17.8$ GPa [44]. Notice that the absence of this phase for the CrNi electrode is likely linked to the oxidation of this electrode as shown by the XRD spectrum (Fig. 4a). The Berkovich hardness associated to the (002) orientation, where $M_{(002)} \cong 340$ GPa, is about $H_{b(002)} = 26 \pm 2$ GPa.

Between the two metal electrodes that have been tested, the CrNi electrode proved to be the best choice since it led to a well (002) orientated AlN film and a well defined value of $M_{(001)}$. The Young's modulus calculated from the C_{ij} values [35] is equal to 333 GPa in the \vec{c} direction, very close to $M_{(001)}$, and equal to 284 GPa in the perpendicular direction.

4.3. Internal thin film stress values

The bending of the test structures cantilevers before and after the AlN deposition on their CrNi and Pt electrodes respectively gave valuable information about the stress levels in the films. The measurements shown in Fig. 6, deflection δ_m as a function of the square length of the cantilever, indicated that the stress in the CrNi film was a tensile one, while the Pt film was under compression, the change of slope after AlN deposition indicates a compressive stress. Numerical calculations using Eqs. (1), (2) and (3) with $\sigma_{Si} = 0$, $E_{Si} = 129$ GPa, $E_{AlN} = 330$ GPa, $E_{CrNi} = 237$ GPa and $E_{Pt} = 168$ GPa with $\nu = 0.3$ led to values of +1110 MPa tensile stress for CrNi and -700 MPa compressive stress for Pt. After its deposition on the two different metal electrodes, the stress value in the AlN film deposited on CrNi was $\sigma_{AlN} = -220$ MPa, versus $\sigma_{AlN} = -564$ MPa for the one deposited on Pt.

CrNi proved again to be a better choice as metal electrode since it allows the deposition of less stressed AlN film. Moreover,

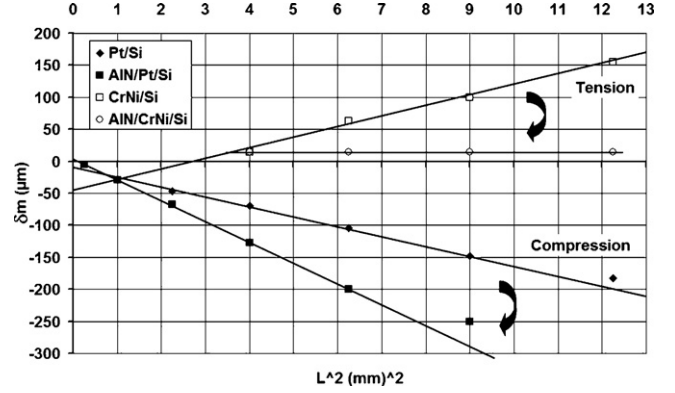


Fig. 6. Measured test structures cantilever bending before and after the deposition of the AlN film as a function of their square length.

if the thickness of the films is well chosen, it is possible to obtain a structure with a global stress equal to zero (at a given constant temperature), $\delta_m \cong 0$, as shown in Fig. 6 with the CrNi electrode.

The compressive stress in the AlN film has been related in the literature to the dc power input [16]. Meng et al. [46] have also shown that the stress was a function of the AlN film thickness: it had a minimum for thickness between 0.5 and 1 μm and it is increasing for greater thickness. These observations have been confirmed in this study. Table 2 gives the calculated AlN stress in the test structures but also in the final devices that had AlN thicknesses of 1 μm (wafer 1) and 1.4 μm (wafer 2). The AlN compressive stress is significantly increasing with its thickness. Therefore, if the aim is to realize an AlN driven structure with low global stress, the CrNi electrodes thicknesses should be adjusted not only to the thickness value, but also to its thickness dependent stress value.

However, in the present study, all the films have been deposited with the same deposition rate $\cong 17$ nm/min, so it is not possible to distinguish the effect of the film thickness from those of the deposition time. During the phase of the process optimization, some experiments have been carried out on AlN deposited on Al/Si electrode [47]. The input power was 150 W leading to a low deposition rate of about 3 nm/min. The AlN film had a thickness of 0.4 μm . Table 2 reports, for all the tested films, the dependence of the σ_{AlN} stress versus the sputtering time t . The residual stress seems to be an increasing function of the deposition time, which indicates that there is a strong link between the film structure and the crystallinity and the film growth mode, in accordance with the results of Auger et al. [14].

Table 2

Internal thin film stress values as a function of the electrode nature, thickness h_f , deposition rate V and deposition time t

| Electrode | h_f (μm) | V (nm/min) | t (min) | N (Meas.) | σ_{AlN} (MPa) |
|-----------|-------------------------|--------------|-----------|-------------|----------------------|
| CrNi | 1.4 | 17 | 74 | 22 | -860 ± 70 |
| CrNi | 1.0 | 17 | 53 | 20 | -314 ± 136 |
| CrNi | 0.8 | 17 | 42 | 2 | -222 |
| Pt | 0.8 | 17 | 42 | 2 | -564 |
| Al | 0.4 | 3 | 133 | 4 | -1082 ± 326 |

N is the number of measurements.

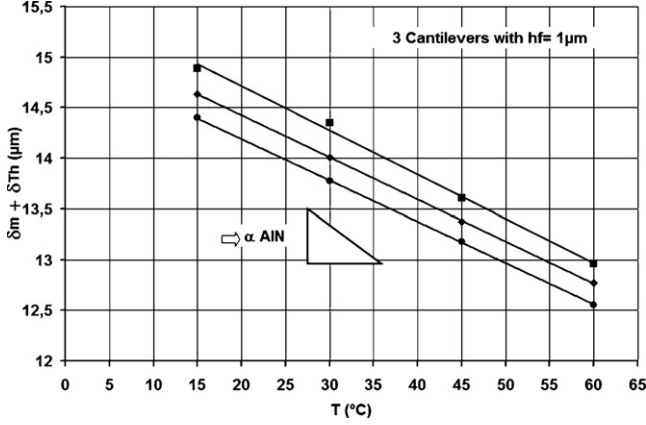


Fig. 7. Static initial deflection as a function of the temperature for three of the 800 μm long cantilevers.

4.4. Thermal expansion coefficient determination

The thermo-electrical module (Peltier device) integrated in the sample holder of the optical profilometer allowed us to control the cantilevers temperature between 15 and 60 $^{\circ}\text{C}$ and thus to determine the thermal expansion coefficient (TEC) of the AlN films (Eq. (8)). Fig. 7 shows the variation of the total deflection $\delta_m + \delta_{Th}$ as a function of the temperature for three different beams. The application of Eq. (8) knowing the slope of these curves ($\Delta\delta_{Th}/\Delta T$) and the material parameters ($h_f = 1 \mu\text{m}$, $h_s = 16.05 \mu\text{m}$, $h_e = 0.506 \mu\text{m}$, $L = 800 \mu\text{m}$, $\alpha_s = 2.44 \times 10^{-6} \text{K}^{-1}$, $\alpha_e = 9.5 \times 10^{-6} \text{K}^{-1}$) allowed us to calculate $\alpha_f = \alpha_{AlN}$. We found $4.3 \times 10^{-6} < \alpha_{AlN} < 4.6 \times 10^{-6} \text{K}^{-1}$, which is in good agreement with the values reported in the literature for bulk material; $4.4 \times 10^{-6} < \alpha_{AlN} < 5.3 \times 10^{-6} \text{K}^{-1}$ [48] and $4.03 \times 10^{-6} < \alpha_{AlN} < 4.84 \times 10^{-6} \text{K}^{-1}$ [49].

4.5. Resonance frequency measurements

A sinusoidal signal (8 V-PP) was applied to the cantilevers through the two electrodes. The enhanced-time average interferometry method was applied to determine the first resonance frequency f_1 of the micro-beams. As shown in Fig. 8a and according to Eq. (6), f_1 is proportional to $1/L^2$; $37 \text{ kHz} < f_1 < 500 \text{ kHz}$ for $200 \mu\text{m} < L < 800 \mu\text{m}$. Similar measurements performed on AlN/Al/Si cantilevers have been also reported previously by Andrei et al. [47].

There is a fairly good agreement between the experimental values and the theoretical ones calculated from Eq. (6) (Fig. 8a), except for the shorter beams where the frequency is very high ($f_1 \cong 500 \text{ kHz}$ for $L = 200 \mu\text{m}$) and the geometrical uncertainties of the beams cannot be neglected.

A more detailed analysis is performed on different cantilevers having the same length, $L = 800 \mu\text{m}$ and coming from wafer 1, $h_f = 1 \mu\text{m}$, 15 tested beams, and wafer 2, $h_f = 1.4 \mu\text{m}$, 22 tested beams. Fig. 8b shows, as a function of the initial deflection δ_m , the experimental and theoretical values of f_1 for the different cantilevers taking into account the precise geometry measured of each cantilever. The theoretical values are always smaller

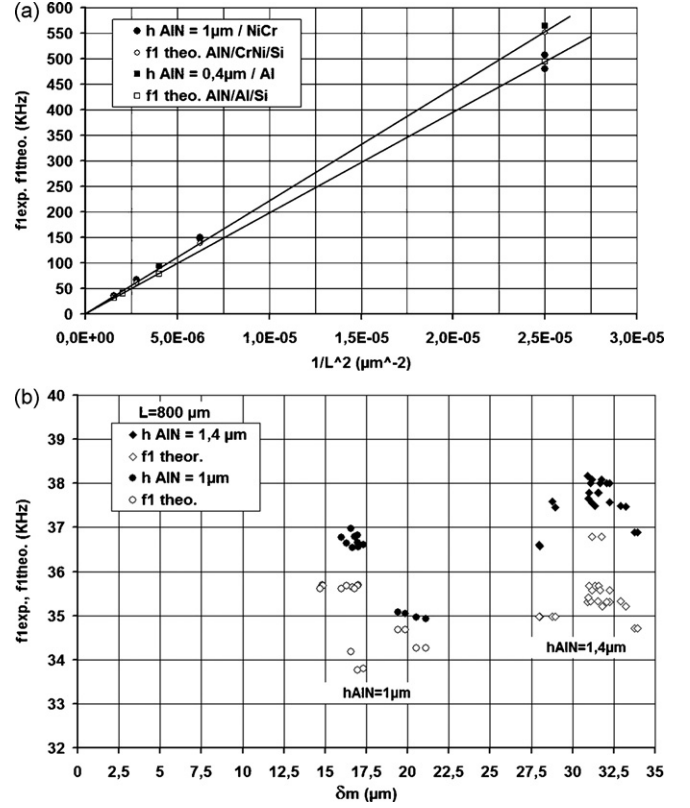


Fig. 8. Measured of the first resonance frequency as a function of the inverse of the square length of the cantilevers (a) or as a function of the initial static deflection of the 800 μm long cantilevers with thickness of 1 and 1.4 μm (b).

than the experimental ones, in an order of 3.1 and 6.5% for wafers 1 or 2, respectively. This difference can be explained by the presence of geometrical imperfections in the neighbourhood of the clamping area, due to small misalignment of the two masks during the anisotropic silicon etching (steps 5–7 in the flow chart). The overflow of the $\langle 111 \rangle$ Si plane under the cantilevers affects the true value of the clamping length and the real values are smaller than those measured on the top side of the beam. To obtain the experimental frequencies, the L values should be around 788 μm ($-12 \mu\text{m}$) and 774 μm ($-26 \mu\text{m}$) for wafer 1 and 2, respectively. It is also observed that, for each wafer, the relative discrepancy between the experimental and theoretical values of f_1 varies approximately as $1/L$ (for example see Fig. 9a, $1/L^2 = 2.5 \times 10^{-5} \mu\text{m}^2$, $L = 200 \mu\text{m}$), which is in accordance with the previous explanations.

4.6. AlN piezoelectric coefficient determination

When a dc voltage is applied between the upper and the lower metal electrodes, ($\pm 15 \text{ V}$ for $h_f = 1.4 \mu\text{m}$ and $\pm 10 \text{ V}$ for $h_f = 1 \mu\text{m}$) a supplementary displacement δp (Eq. (5)) must be added to the stress induced mechanical bending δm (Eq. (1)). As shown in Fig. 9a, the measured piezoelectric displacement δp is linearly dependent on the applied voltage. The slope for the wafer 2 sample is greater since the AlN film is much thicker than for the wafer 1 devices (the silicon and metal electrodes have the same thickness for both wafers).

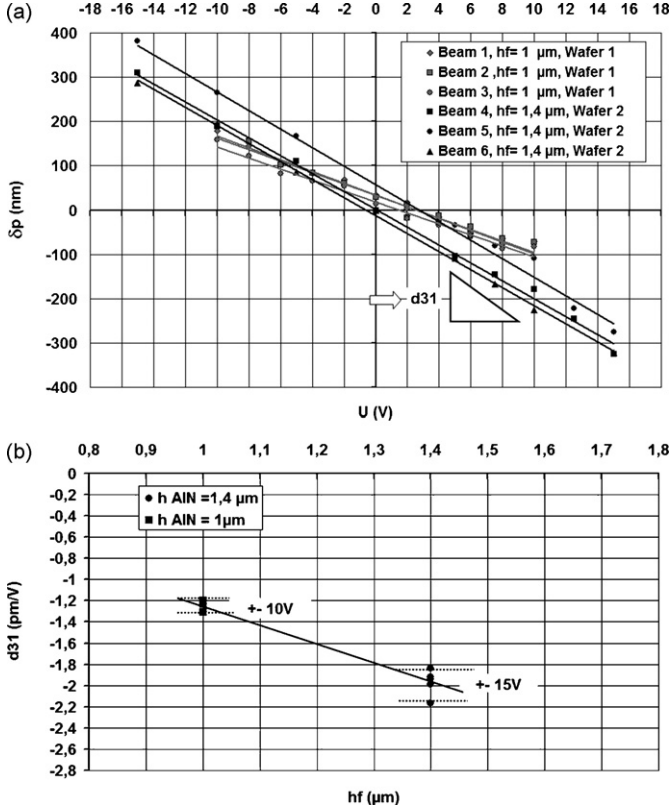


Fig. 9. Measured piezoelectric induced displacement variation with the applied voltage for 800 μm long cantilever samples with 1 and 1.4 μm AlN thickness (a), d_{31} piezoelectric coefficient value as a function of the AlN film thickness (b).

However, this different slope is not only related to the different thickness. Using Eq. (5) and as shown in Fig. 9b for different cantilevers, the piezoelectric coefficient d_{31} value for wafer 2 (1.4 μm AlN) was found to be -2.0 ± 0.15 pm/V, for only -1.3 ± 0.1 pm/V for the wafer 1 samples (1 μm AlN). The first -2.0 pm/V value is in good agreement with d_{31} coefficients measured on pulsed reactive dc sputtered AlN films, $d_{31} = -2.0 \pm 0.1$ pm/V and $d_{31} = -1.6 \pm 0.1$ pm/V for films grown at 200 and 90 $^{\circ}\text{C}$, respectively [50], $d_{31} = -1.8 \pm 0.1$ pm/V for films grown by molecular beam epitaxy [51]. In this study all films were deposited on substrate, which restricts the strain in the plane of the films and thus reduces the strain along the \bar{c} axis. So, the clamped coefficient d_{13}^c measured on these films is smaller than the value for the unconstrained bulk material d_{13}^b . Moreover, for Wurtzite crystals, $d_{31} = -(1/2)d_{33}$ and it is thus possible [50,51] to calculate d_{33}^b from the d_{13}^c coefficient of the films by the relation:

$$d_{33}^b = -2d_{13}^c \left(\frac{S_{11}^E + S_{12}^E}{S_{11}^E + S_{12}^E + \alpha S_{13}^E} \right) \quad (14)$$

α is a factor depending of the clamping amount ($0 \leq \alpha \leq 1$) and the S_{ij} parameters are the elastic compliances at constant electric field. They are calculated from the C_{ij} values given in Table 1 [35,36]. The numerical application of Eq. (14) for a perfect clamping $\alpha = 1$, gives: $d_{33}^b = 5.7$ pm/V for $d_{13}^c = -2$ pm/V (1.4 μm AlN) but only $d_{33}^b = 3.7$ pm/V for $d_{13}^c = 1.3$ pm/V.

(1 μm AlN). The first value of d_{33}^b is very close to those reported for bulk material; $d_{33}^b = 5.6$ pm/V [50] and $d_{33}^b \cong 5.0$ pm/V [52]. 3D finite element calculation (ANSYS) performed with the C_{ij} values given in Table 1 (sputtered high quality), $d_{13} = (-1/2)d_{33}$, $d_{15} = 4$ pm/V [35], the true thickness of the different films, $h_{\text{Sup}} = 0.35$ μm , $h_{\text{Inf}} = 0.15$ μm , $h_{\text{AlN}} = 1.4$ μm , $h_{\text{Si}} = 15.19$ μm and $L = 800$ μm , $l = 50$ μm , allows to determine $d_{13} = -2.2$ pm/V, which is close to the analytical value $d_{13} = -2.0$ pm/V calculated from Eqs. (5) and (14) with $\alpha = 1$.

However, for wafer 1, the d_{33}^b value is some-how small compared to those of bulk material, which indicates that the AlN deposition process needs further optimization. Another possible explanation could be the influence of the dependence of α with the film thickness. The factor α is greater for smaller thickness, so for the same value of d_{33}^b , d_{13}^c decreases with α since S_{13} is negative. This could indicate a relationship between the deposited AlN thickness and its piezoelectric properties.

4.7. Joule effect on some cantilevers

Impedance measurements (R) on all wafers 1 and 2 devices have been performed. They showed that some of the different cantilevers arrays present on each device were in short cut. When a voltage was applied to these cantilevers they had an important displacement $\delta \gg \delta_p$ proportional to the square of the voltage

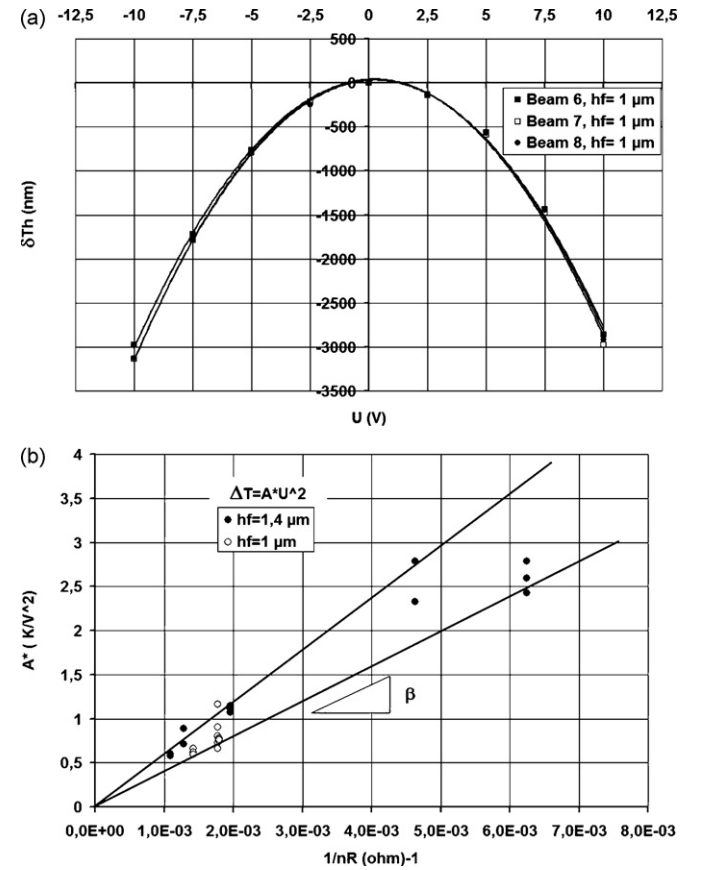


Fig. 10. Measured induced displacement variation with the applied voltage for 800 μm long cantilever samples in short cut (a), evolution of the coefficient A_{exp}^* with the inverse of the device resistance (b).

(Fig. 10a), that has a Joule effect origin. Note that 15 V applied bias has proved to be too high for some of the cantilevers with $h_f = 1 \mu\text{m}$ leading to severe damage of the electrodes and the AlN beneath it. After this damage it was observed important parabolic bending related to the heating of the AlN and Si films thanks to the electrodes.

From Fig. 10a, we can deduce the relation:

$$\delta_{\text{Th}} = A_{\text{exp}} U^2 \quad (15)$$

which combined with Eq. (5) leads to:

$$\begin{aligned} \Delta T &= \frac{E_{\text{eq}} h_{\text{eq}}^3 (E_f h_f + E_s h_s + E_e h_e)}{3[E_s h_s^2 - (E_f h_f + E_e h_e)(h_e + h_f)]} A_{\text{exp}} U^2 \\ &\quad \times [\alpha_s (E_f h_f + E_e h_e) - (E_f \alpha_f h_f + E_e \alpha_e h_e)] L^2 \\ &= A_{\text{exp}}^* U^2 \end{aligned} \quad (16)$$

If we consider the very simple thermal conduction model of a wall heated on one side by an electric resistance r , then: $\Delta T = \beta(U^2/r)$, and since the resistances of each beam are associated in parallel configuration:

$$A_{\text{exp}}^* = \frac{\beta}{nR} \quad (17)$$

The representation $A_{\text{exp}}^* = f(1/nR)$ for all the tested arrays in short cut is given on Fig. 10b. The slope of these curves gives $390 < \beta < 590 \text{ K/W}$.

5. Conclusions

The presented process allowed the fabrication of AlN driven cantilevers that present good piezoelectrical behaviour. CrNi proved to be a better choice as bottom electrode, since the AlN deposited on it had better (002) orientation, a well defined Young's modulus and lower stress. The influence of AlN thickness on its stress level has also been investigated, the obtained results giving reliable information in designing AlN driven structures with a low global stress. The thermal expansion coefficient of these films has been determined. The devices obtained from the wafer with a thicker AlN film (1.4 μm) showed better piezoresistive properties, with a d_{31} coefficient of -2.0 pm/V . All the physical parameters have been calculated using non approximated analytical equations. From a material point of view, the important result is that the well oriented (002) AlN ceramic thin films exhibit approximately the same electro-thermo-mechanical properties, C_{ij} , α , d_{31}^b as the bulk material.

References

[1] M. Clement, L. Vergara, J. Sangrador, E. Iborra, A. Sanz-Hervas, SAW characteristics of AlN films sputtered on silicon substrates, *Ultrasonics* 42 (2004) 403–407.
[2] T. Palacios, F. Calle, E. Monroy, J. Grajal, M. Eickhoff, O. Ambacher, C. Prieto, Nanotechnology for SAW devices on AlN epilayers, *Mat. Sci. Eng. B* 93 (2002) 154–158.
[3] Ju-Hyung Kim, Si-Hyung Lee, Jin-Ho Ahn, Jeon-Kook Lee, AlN piezoelectric materials for wireless communication thin film components, *J. Ceram. Process. Res.* 3 (1) (2002) 25–28.

[4] K.M. Lakin, J. Belsick, J.F. McDonald, K.T. McCarron, Improved bulk wave resonator coupling coefficient for wide bandwidth filters, *IEEE Ultrasonics Symp.* (October) (2001) 3E–5E.
[5] A. Choujaa, N. Tirole, C. Bonjour, G. Martin, D. Hauden, P. Blint, A. Cachard, C. Pommier, AlN/silicon lamb-wave microsensors for pressure and gravimetry measurements, *Sens. Actuators A* 46–47 (1995) 179–182.
[6] T. Laurent, F.O. Bastien, J.-C. Pommier, A. Cachard, D. Remiens, E. Cattan, Lamb wave and plate mode in ZnO/silicon and AlN/silicon membrane. Application to sensors able to operate in contact with liquid, *Sens. Actuators A* 87 (2000) 26–37.
[7] D. Ruffieux, M.A. Dubois, N.F. de Rooij, An AlN piezoelectric microactuator array, in: *IEEE MicroElectro Mech. Syst.*, Miyazaki, Japan, Jan. 23–27, 2000, pp. 662–667.
[8] M.A. Dubois, P. Muralt, Properties of AlN thin films for piezoelectric transducers and microwave filter applications, *Appl. Phys. Lett.* 74 (20) (1999) 3032–3034.
[9] S. Bargiel, D. Heinis, C. Gorecki, A. Górecka-Drzazga, J.A. Dziuban, M. Józwick, A micromachined silicon-based probe for a scanning near-field optical microscope on-chip, *Meas. Sci. Tech.* 17 (2006) 32–37.
[10] M. Ishihara, S.J. Li, H. Yumoto, K. Akashi, Y. Ide, Control of preferential orientation of AlN films prepared by the reactive sputtering method, *Thin Solid Films* 316 (1998) 152–157.
[11] X.H. Xu, H.S. Wu, C.J. Zhang, Z.H. Jin, Morphological properties of AlN piezoelectric thin films deposited by DC reactive magnetron sputtering, *Thin Solid Films* 388 (2001) 62–67.
[12] M. Akiyama, C.N. Xu, K. Nonaka, K. Shoku, T. Watonabe, Statistical approach for optimizing sputtering conditions of highly oriented aluminium nitride thin films, *Thin Solid Films* 315 (1998) 62–65.
[13] K. Kusaka, D. Taniguchi, T. Hanakusa, K. Tomiraga, Effect of input power on crystal orientation and residual stress in AlN film deposited by DC sputtering, *Vacuum* 59 (2000) 806–813.
[14] M.A. Auger, L. Vazquez, M. Jergel, O. Sanchez, J.M. Albella, Structure and morphology evolution of AlN films grown by DC sputtering, *Surf. Coat. Tech.* 180–181 (2004) 140–144.
[15] V.M. Pantojas, W. Otano-Rivera, J.W. Caraballo, Statistical analysis of the effect of deposition parameters on the preferred orientation of sputtered AlN films, *Thin Solid Films* 492 (2005) 118–123.
[16] M. Józwick Gorecki, L. Salbut, Multifunctional interferometric platform for on-chip testing the micromechanical properties of MEMS/MOEMS, *J. Microlithography Microfabrication Microsyst.* 4 (2005) 1–10.
[17] L. Salbut, K. Patorski, M. Józwick, J. Kacperski, C. Gorecki, A. Jacobelli, T. Dean, Active microelement testing by interferometry using time-average and quasi-stroboscopic techniques, *SPIE Microsyst. Eng.: Metrol. Inspect. III* 5145 (2003) 23–32.
[18] W.C. Oliver, G.M. Pharr, An improved technique for determining hardness and elastic modulus using load and displacement sensing indentation experiments, *J. Mater. Res.* 1 (1992) 1564–1583.
[19] M.S. Bobji, S.K. Biswas, Hardness of a surface containing uniformly spaced pyramidal asperities, *Trib. Lett.* 7 (1999) 51–56.
[20] M. Qasmi, P. Delobelle, Influence of the average roughness R_{ms} on the precision of the Young's modulus and hardness determination using nano-indentation technique with a Berkovich indenter, *Surf. Coat. Tech.* 201 (2006) 1191–1199.
[21] G.G. Stoney, The tension of metallic films deposited by electrolysis, *Proc. R. Soc. Lond., Ser. A* 82 (1909) 172.
[22] K. Röhl, Analysis of stress and strain distribution in thin films and substrates, *J. Appl. Phys.* 47 (7) (1976) 3224–3229.
[23] P.H. Townsend, D.M. Barnett, T.A. Brunner, Elastic relationships in layered composite media with approximation for the case of thin films on a thick substrate, *J. Appl. Phys.* 62 (11) (1987) 4438–4444.
[24] J.H. Jou, L. Hsu, Stress analysis of elastically anisotropic bilayer structures, *J. Appl. Phys.* 69 (3) (1991) 1384–1388.
[25] J.G. Smits, W.S. Choi, The constituent equations of piezoelectric heterogeneous bimorphs, *IEEE Trans. Ultrason., Ferroelectr. Freq. Control* 38 (3) (1991) 256–270.
[26] Q.M. Wang, L.E. Cross, Constitutive equations of symmetrical triple layer piezoelectric benders, *IEEE Trans. Ultrason., Ferroelectr. Freq. Control* 46 (6) (1999) 1343–1351.

- [27] K. Yao, W. Zhu, K. Uchino, Z. Zhang, L.C. Lim, Design and fabrication of a high performance multilayer piezoelectric actuator with bending deformation, *IEEE Trans. Ultrason., Ferroelectr. Freq. Control* 46 (4) (1999) 1020–1027.
- [28] S.H. Chang, C.C. Chou, Electromechanical analysis of an asymmetric piezoelectric elastic laminate structure: theory and experiment, *IEEE Trans. Ultrason., Ferroelectr. Freq. Control* 46 (2) (1999) 441–451.
- [29] V. Walter, Thesis Univ. Franche-Comté, Caractérisation et modélisation électromécanique de dépôts de couches épaisses sérigraphiées sur substrat d'alumine, Application au control de forme et à l'amortissement actif d'un bimorphe (2001).
- [30] V. Walter, P. Delobelle, P. Le Moal, E. Joseph, E. Collet, A piezomechanical characterization of PZT thick films screen-printed on alumina substrate, *Sens. Actuators A* 96 (2002) 157–166.
- [31] J.J. Vlassak, W.D. Nix, Measuring the elastic properties of anisotropic materials by means of indentation experiments, *J. Mech. Phys. Sol.* 42 (8) (1994) 1223–1245.
- [32] J.J. Vlassak, W.D. Nix, Indentation modulus of elastically anisotropic half-spaces, *Phil. Magn. A* 67 (5) (1993) 1045–1056.
- [33] A. Delafargue, F.J. Ulm, Explicit approximations of the indentation modulus of elastically orthotropic solids for conical indenters, *Int. J. Solids Struct.* 41 (2004) 7351–7360.
- [34] P. Delobelle, E. Fribourg-Blanc, D. Remiens, Mechanical properties determined by nanoindentation tests of PZT and PMNT sputtered thin films, *Thin Solid Films* 515 (2006) 1385–1393.
- [35] G. Carlotti, F.S. Hickernell, H.M. Liaw, L. Palmieri, G. Socino, E. Verona, The elastic constants of sputtered aluminium nitride films, *IEEE Ultrason. Symp.* (1995) 353–356.
- [36] K. Tsubouchi, K. Sugai, N. Mikoshida, AlN material constants evaluation and SAW properties on AlN/Al₂O₃ and AlN/Si, *IEEE Ultrason. Symp.* (1981) 375–380.
- [37] A.F. Wright, Elastic properties of zinc-blende and wurtzite AlN, GaN and InN, *J. Appl. Phys.* 82 (6) (1997) 2833–2839.
- [38] L. Robert, P. Delobelle, Internal report, unpublished work (2001).
- [39] R.B. King, Elastic analysis of some punch problems for layered medium, *Int. J. Solids Struct.* 23 (1987) 1657–1664.
- [40] R. Saha, W.D. Nix, Effects of the substrate on the determination of thin film mechanical properties by nano-indentation, *Acta Mater.* 50 (2002) 23–28.
- [41] Z. Xue, Y. Huang, K.C. Hwang, M. Li, The influence of indenter tip radius on the micro-indentation hardness, *J. Eng. Mat. Tech.* 124 (2002) 371–379.
- [42] Q.M. Wang, Y. Ding, Q. Chen, M. Zhao, J. Cheng, Crystalline orientation dependence of nanomechanical properties of Pb (Zr Ti) O₃ thin films, *Appl. Phys. Lett.* 86 (2005) 162–903.
- [43] P. Delobelle, G.S. Wang, E. Fribourg-Blanc, D. Remiens, Indentation modulus and hardness of Pb(Zr-Ti)O₃ sol-gel films deposited on Pt and LaNiO₃ electrodes. An estimation of the C_{ij} compliances, *J. Eur. Ceram. Soc.* 27 (2007) 223–230.
- [44] W. Xiao, X. Jiang, Optical and mechanical properties of nanocrystalline aluminium oxy-nitride films prepared by electron cyclotron resonance plasma enhanced chemical vapor deposition, *J. Cryst. Growth* 264 (2004) 165–171.
- [45] S. Dagdag, J. Alexis, J.D. Beguin, J.A. Petit, M. Ferrato, J. Durand, Propriétés mécaniques de revêtements d'AlN sur carbure de Silicium fritté par dépôt chimique en phase vapeur assisté plasma, *Matériaux* 2006, 13–17 Nov. 2006, Dijon, France.
- [46] W.J. Meng, J.A. Sell, G.L. Eesley, T.A. Perry, Measurement of intrinsic stresses during growth of aluminium nitride thin films by reactive sputter deposition, *J. Appl. Phys.* 74 (4) (1993) 2411–2414.
- [47] A. Andrei, K. Krupa, M. Jozwik, L. Nieradko, C. Gorecki, L. Hirsinger, P. Delobelle, Fabrication, characterization and reliability study of AlN driven cantilevers, *Proc. SPIE* 6188 (April 2006) (2006), Strasbourg.
- [48] http://www.ceramic-center.com/cttc_pdf/nitride_al.pdf.
- [49] MEMS and Nanotechnology Clearinghouse, www.memsnetwork.org/material/aluminiumnitride, MEMS Exchange (2001).
- [50] L.L. Guy, S. Muensit, E.M. Goldys, Extensional piezoelectric coefficients of gallium nitride and aluminium nitride, *Appl. Phys. Lett.* 75 (26) (1999) 4133–4135.
- [51] C.M. Lueng, H.L.W. Chan, S. Surya, C.L. Choi, Piezoelectric coefficient of aluminium nitride and gallium nitride, *J. Appl. Phys.* 88 (9) (2000) 5360–5363.
- [52] C.J. Ho, T.K. Shing, P.C. Li, Preferred orientation control and characterization of AlN thin films using reactive sputtering, *Tamkang J. Sci. Eng.* 7 (1) (2004) 1–4.